Technical note: Measurement of chemically-resolved volume equivalent diameter and effective density of particles by AAC-SPAMS

Long Peng[1,2], Lei Li[4], Guohua Zhang[1, 3*], Xubing Du[4], Xinming Wang[1, 3], Ping'an Peng[1, 3], Guoying Sheng[1], Xinhui Bi[1, 3*]

[1] State Key Laboratory of Organic Geochemistry and Guangdong Provincial Key Laboratory of Environmental Protection and Resources Utilization, Guangzhou Institute of Geochemistry, Chinese Academy of Sciences, Guangzhou 510640, China

[2] University of Chinese Academy of Sciences, Beijing, 100049, China

[3] Guangdong-Hong Kong-Macao Joint Laboratory for Environmental Pollution and Control, Guangzhou 510640, China

[4] Institute of Mass Spectrometer and Atmospheric Environment, Jinan University, Guangzhou 510632, China

*Correspondence to: bixh@gig.ac.cn and zhanggh@gig.ac.cn

Abstract

Size and effective density (ρ_e) are important properties of aerosol particles and are related to their influences on human health and the global climate. The volume equivalent diameter (D_{ve}) is an intrinsic property that is used to evaluate particle size. ρ_e, defined as the ratio of particle density to a dynamic shape factor (χ), is used to characterize the physical property of a particle as an alternative to particle density. However, it is still challenging to simultaneously characterize the D_{ve} and ρ_e of particles. Here, we present a novel system that classifying particles with their aerodynamic diameter (D_a) by aerodynamic aerosol classifiers (AAC) and determining their vacuum aerodynamic diameter (D_{va}) by single particle aerosol mass spectrometry (SPAMS) to achieve a measurement of D_{ve} and ρ_e. The reliability of the AAC-SPAMS system for accurately obtaining D_{ve} and ρ_e is verified based on the results that the deviation between the measured values and the theoretical values is less than 6% for the size-resolved spherical polystyrene latex (PSL). The AAC-SPAMS system is applied to characterize the D_{ve} and ρ_e of $(NH_4)_2SO_4$ and $NaNO_3$ particles, suggesting that these particles are aspherical and their ρ_e are independent of particle size. Finally, the AAC-SPAMS system is deployed in a field measurement, showing that it is a powerful technique to characterize the chemically-resolved D_{ve} and ρ_e of particles in real time.

1. Introduction

Size and particle density (ρ_p) are critical parameters of aerosol particles in quantifying the impact of aerosols on air quality, human health and global climate change (Buseck and Posfai, 1999; Poschl, 2005; Pitz et al., 2003). Effective density (ρ_e) has been adopted to characterize the physical property of a particle as an alternative to ρ_p, since ρ_p for aspherical aerosol particles is hardly measured (Sumlin et al., 2018; Katrib et al., 2005). Size and ρ_e govern the transport properties of a particle both in the atmosphere and in the human respiratory system (Seinfeld and Pandis, 1998; Liu and Daum, 2008) and directly/indirectly influence the potential of the particle to absorb or reflect solar radiation (Tang, 1997; Zhao et al., 2019; Liu and Daum, 2008). ρ_e can also provide information concerning particle morphology (Yon et al., 2015) and serve as a tracer for atmospheric processing (Guo et al., 2014; Yin et al., 2015; Liu et al., 2015). However, the quantitative relationship between aerosol properties, namely, size and ρ_e, and their effects on air quality, human health and global climate change is not yet well understood, which is partly because important aerosol properties cannot be measured by current techniques.

Size. Size is a fundamental property of particles, which can be parameterized by the physical quantity of volume equivalent diameter (D_{ve}). Defined as the diameter of a spherical particle with the same volume as the particle (DeCarlo et al., 2004), D_{ve} is an intrinsic physical quantity that can be used to evaluate the actual size of the particle. However, to date, atmospheric science usually describes particle size by other diameter definitions, such as the electric mobility diameter (D_m), aerodynamic equivalent

57   diameter (D_a) and vacuum aerodynamic equivalent diameter (D_{va}), whose relationships

58   with D_{ve} are shown in Eqs. (1)-(3), respectively:

59
$$\frac{D_m}{C_c(D_m)} = \frac{D_{ve}}{C_c(D_{ve})} \chi_t, \tag{1}$$

60
$$D_a = D_{ve} \sqrt{\frac{\rho_p C_c(D_{ve})}{\chi_t \cdot \rho_0 \cdot C_c(D_a)}}, \tag{2}$$

61
$$D_{va} = \frac{\rho_p}{\rho_0} \frac{D_{ve}}{\chi_v}, \tag{3}$$

62   where $C_c(D)$ is the Cunningham slip correction factor, χ_t and χ_v represent the aerosol

63   dynamic shape factor (χ) in the transition regime and in the free-molecule regime,

64   respectively, and ρ_0 represents the unit density of 1.0 g/cm^3. From the definitions, it can

65   be seen that D_m, D_a, and D_{va} are originally derived from D_{ve}, but in actuality, they do

66   not reflect the actual size of the particle. Meanwhile, D_{ve} cannot be easily obtained,

67   which limits its application in the scientific community.

68   **Effective density.** At present, three definitions of ρ_e are introduced in atmospheric

69   science (DeCarlo et al., 2004): the first definition (ρ_e^I) is the ratio of the measured

70   particle mass (m_p) to the particle volume (V) calculated assuming a spherical particle

71   with a diameter equal to the measured D_m; the second definition (ρ_e^{II}) is the ratio of ρ

72   to χ (Hand and Kreidenweis, 2002); and the third definition (ρ_e^{III}) is the ratio of D_m and

73   D_{va}, all of which are expressed in Eqs. (4)-(6), respectively.

74
$$\rho_e^I = \frac{6 m_p}{\pi D_m^3} \tag{4}$$

75
$$\rho_e^{II} = \frac{\rho_p}{\chi} \tag{5}$$

76
$$\rho_e^{III} = \frac{D_{va}}{D_m} \rho_0 \tag{6}$$

77   The definitions of ρ_e^I and ρ_e^{III} can be derived into the final forms, as shown in the Eqs.(7)

78   and (8), respectively.

79
$$\rho_e^{\text{I}} = \frac{\rho}{\chi_t^{3}} \cdot \left(\frac{C_c(D_{ve})}{C_c(D_m)}\right)^{3} \tag{7}$$

80
$$\rho_e^{III} = \rho \cdot \frac{C_c(D_{ve})}{\chi^2 \cdot C_c(D_m)} \tag{8}$$

81   The Eq. (7) is derived from combining the Eq. (1) with Eq. (4) in which m_p is equal to

82    $1/6\ \rho \cdot D_{ve}^{3}$. The detailed derivation of Eq. (8) was presented in Schneider et al.

83   (2006). The ρ_e^{I} and ρ_e^{III} are demonstrated to have the inherent characteristics of

84   decreasing with increasing particle size in a separate paper. Therefore, it will introduce

85   systemic error when assessing the particle impacts on visibility, human health and

86   climate from the physical quantities in ρ_e^{I} and ρ_e^{III}. In contrast, ρ_e^{II} is independent of

87   particle size. Previously, ρ_e^{II} and the real part in the refractive index (n) can be retrieved

88   from a fitting procedure that compares the measured light-scattering intensity of

89   particles (R_{meas}) to the theoretical values ($R_{theory,test}$) calculated by a series of n and ρ_e^{II}

90   values. Moffet and Prather (2005) successfully obtained ρ_e^{II} for spherical particles by

91   single particle mass spectrometry. However, subject to the accuracy of Mie theory for

92   the aspherical particles, dry NaCl and calcium-rich dust particles were failed to fit the

93    $R_{theory,test}$ well to R_{meas} (Moffet et al., 2008). Similarly, Zhang et al. (2016a) failed to

94   simultaneously retrieve ρ_e^{II} and n for $(NH_4)_2SO_4$ and $NaNO_3$ particles. To our best

95   knowledge, there is no effective technique to achieve the measurement of ρ_e^{II} for

96   aspherical particles. For reference, the symbol ρ_e in the following text refers to the

97   definition of ρ_e^{II}.

98   The aim of the present work is to develop a method to obtain D_{ve} and ρ_e. The

99   established system of an aerodynamic aerosol classifier (AAC)-single particle aerosol

100   mass spectrometry (SPAMS) is capable of characterizing the D_a and D_{va} of particles,

101 which can be applied to theoretically derive D_{ve} and ρ_e. To verify the reliability of the

102 AAC-SPAMS system, we apply it to measure the D_{ve} and ρ_e of the spherical particles

103 of polystyrene latex (PSL). The results are in good agreement with the theoretical values.

104 Finally, the AAC-SPAMS system is applied to measure the D_{ve} and ρ_e for $(NH_4)_2SO_4$

105 and $NaNO_3$ particles and for the chemically-resolved atmospheric particles.

106

107 **2. Experimental section**

108 **2.1 Measurement system**

109 Figure 1 shows a schematic diagram of the AAC-SPAMS system. The particles are

110 first dried by a diffusion drying tube (TSI 9302, USA), classified by AAC (Cambustion

111 Ltd., UK) based on the aerodynamic diameters D_a, and then transported into SPAMS in

112 which the D_{va} and the mass spectra of individual particles are obtained. The working

113 principle of the AAC is described in detail elsewhere (Tavakoli and Olfert, 2013). AAC

114 consists of two coaxial cylinders that rotate at the same rotational speed. Polydisperse

115 particles enter into the space between the cylinders (i.e., classification column) and

116 experience a centrifugal force that causes them to move toward the outer cylinder. The

117 particles to be classified can leave the classification column with the particle-free sheath

118 flow and finally exit the AAC with the sample flow. Thus, the D_a values of classified

119 particles can be derived from their relationship with their relaxation time (τ), as shown

120 in Eq. (9):

121 $$\tau = \frac{C_C(D_a) \cdot \rho_0 \cdot D_a^2}{18\mu} \tag{9}$$

122 where μ is the gas dynamic viscosity. Particles with large relaxation times impact and

123   adhere to the outer cylinder, while particles with small relaxation times exit the

124   classifier with the exhaust flow. The exhaust flow from the AAC was about 0.3 lpm,

125   and the Size Resolution Parameter (Rs) of the AAC was set as 40.

126   Detailed information about the operation of SPAMS (Hexin Analytical Instrument

127   Co., Ltd., China) is described elsewhere (Li et al., 2011). Briefly, the particles are

128   introduced into the vacuum system through a 0.1 mm critical orifice and are gradually

129   collimated into a beam in the aerodynamic lens. Two continuous diode Nd:YAG laser

130   beams (532 nm) are used to aerodynamically size the particles, which are subsequently

131   desorbed/ionized by a pulsed laser (266 nm) that is triggered based on the velocity of a

132   specific particle. The generated positive and negative ions are recorded with the

133   corresponding particle size. The D_{va} of the particle is related to the transit time between

134   the two laser beams (532 nm) in SPAMS, which can be obtained by using a calibration

135   curve generated from the measured transit times of a PSL series with predefined sizes

136   (nominal diameters).

137

138   **2.2 Laboratory experiments**

139   Dried spherical PSL (Nanosphere Size Standards, Duke Scientific Corp., Palo Alto)

140   ($\rho_p = 1.055$ g/cm^3 and $\chi = 1.0$) with D_{ve} values of 203.0 ± 5.0 nm, 310.0 ± 6.0 nm, 510.0

141   ± 5.0 nm, and 740.0 ± 6.0 nm were used in the AAC-SPAMS system, and the D_{ve} was

142   verified by Scanning Mobility Particles Sizer (Model 3938, TSI Inc., USA). The PSL

143   particles were first classified by AAC, and then their D_{va} values were obtained by

144   SPAMS. ACC-SPAMS was also applied to the particles of $(NH_4)_2SO_4$ ($\rho_p = 1.77$ g/cm^3)

145 and NaNO$_3$ (ρ_p = 2.26 g/cm^3) with D_a values of 250.0 nm, 350.0 nm, 450.0 nm and

146 550.0 nm.

147 **2.3 Ambient sampling**

148   For field observations, the AAC-SPAMS system was placed in science and

149 technology enterprise accelerator A2 Block, Guangzhou, China, to characterize the D_{ve},

150 ρ_e and chemical compositions of aerosol particles. The sampling inlet was hung 2.5

151 meters from the third floor (~12 m above ground level). Ambient aerosol particles were

152 introduced into the AAC through a 5 m long conductive silicone tube with an inner

153 diameter of 6 mm and a PM$_{2.5}$ cyclone inlet. The overall sampling flow was 3 lpm, and

154 the residence time was approximately 5 seconds. Sampled particles were classified by

155 the AAC as one of four D_a: 250.0 nm, 350.0 nm, 450.0 nm and 550.0 nm. The sampling

156 time for the particles of each D_a was approximately 10 minutes. From July 6th to 8th,

157 2019, approximately 129,869 ionized particles were obtained from nine rounds of

158 measurement. The sampling details are shown in Table S1. The number of ionized

159 particles with the D_a of 250.0, 350.0, 450.0, and 550.0 nm is about 35,609, 38,374,

160 31,910, and 23,976, respectively. The sampled ~100,000 particles are first classified by

161 using an adaptive resonance theory neural network (ART-2a) (Song et al., 1999) with a

162 vigilance factor of 0.75, a learning rate of 0.05 and 20 iterations.

163

164 **2.4 Theoretical derivation of D_{ve} and ρ_e from D_a and D_{va}**

165   D_{ve} is the accurate physical quantity of the size of a particle. ρ_e is an alternative

166 property for ρ_p, which is consistent with the property of ρ_p in terms of being independent

167   of particle size. These two properties cannot yet be measured for unknown particles by

168   current techniques. In this study, the calculations of D_{ve} and ρ_e for unknown particles

169   are theoretically derived from D_a and D_{va}. Combining Eqs. (2) and (3), we obtain the

170   following Eq. (10):

171 $$C_c(D_a)\frac{D_a^{\ 2}}{D_{va}} = D_{ve}C_c(D_{ve})\frac{\chi_v}{\chi_t} \tag{10}$$

172   Based on the approximation between χ_v and χ_t ($\chi_v \approx \chi_t = \chi_a$) (DeCarlo et al., 2004), Eq.

173   (10) becomes Eq. (11):

174 $$C_c(D_a)\frac{D_a^{\ 2}}{D_{va}} = D_{ve}C_c(D_{ve}) \tag{11}$$

175   The Cunningham Slip Correction Factor is calculated by Eq. (12):

176 $$C_c(D) = 1 + \frac{\lambda}{D}\left(A + B \cdot \exp\left(\frac{C \cdot D}{\lambda}\right)\right), \tag{12}$$

177   where λ is the mean free path of the gas molecules, and A, B and C are empirically

178   determined constants specific to the analysis system. Substituting Eq. (12) into Eq. (11)

179   obtains the Eq. (13).

180 $$\frac{D_a^{\ 2}}{D_{va}} + \frac{D_a \cdot \lambda}{D_{va}}\left(A + B \cdot \exp\left(\frac{C \cdot D_a}{\lambda}\right)\right) = D_{ve} + \lambda\left(A + B \cdot \exp\left(\frac{C \cdot D_{ve}}{\lambda}\right)\right) \tag{13}$$

181   Thus, if the D_a and D_{va} of an unknown particle can be measured, its D_{ve} will be

182   calculated according to Eq. (13). Finally, the ρ_e value of the particles is calculated by

183   the D_{va} and D_{ve} values according to Eq. (14), which is obtained by combining Eq.(3)

184   and Eq.(5):

185 $$\rho_e = \frac{\rho_p}{\chi_a} = \frac{D_{va}}{\rho_0 \cdot D_{ve}} \tag{14}$$

186   Thus, we can obtain both the D_{ve} and ρ_e values of unknown particles based on the D_a

187   and D_{va} values. Because the AAC and SPAMS instruments have the ability to determine

188   D_a and D_{va}, the AAC-SPAMS system, which is developed in this study, can be used to

189   obtain the D_{ve} and ρ_e values for unknown particles.

190

191   **3.   Results and discussion**

192   **3.1 Verification of the AAC-SPAMS system to obtain D_{ve} and ρ_e**

193   The D_{va} distribution of PSL particles with predefined D_{ve} values after screening by

194   the AAC is shown in Figure S1. We used Gaussian fitting to obtain the peak D_{va} for

195   each size PSL with an R-squared fitting coefficient (R^2) over 0.98. Each fitting has a

196   full width at half maximum (FWHM) of 6.6%, 4.4%, 2.3% and 2.2%, and the

197   corresponding peaks are 215.8 nm, 319.0 nm, 532.1 nm and 803.5 nm, respectively.

198   Substituting the D_a and D_{va} values of PSL into Eq. (11), the measured D_{ve} ($D_{ve,me}$) of

199   PSL from AAC-SPAMS system is 203.6 nm, 309.7 nm, 511.6 nm and 737.2 nm,

200   respectively (Figure 2a). Thus, the deviations between the theoretical D_{ve} ($D_{ve,th}$) and

201    $D_{ve,me}$ values are 0.3%, -0.1%, 0.3% and -0.4%, respectively. On the other hand, the

202   measured ρ_e ($\rho_{e,me}$) values of the particles are calculated from the D_{va} and $D_{ve,me}$ values

203   with Eq. (14), and the $\rho_{e,me}$ values are 1.1 g/cm^3, 1.0 g/cm^3, 1.0 g/cm^3, and 1.1 g/cm^3

204   (Figure 2b). The deviations of $\rho_{e,me}$ are determined to be 4.3%, -5.2%, -5.2%, and 4.3%,

205   respectively, by comparing to the theoretical ρ_e ($\rho_{e,th}$) that is equals to the ρ_p for the

206   spherical particles (i.e. 1.055 g/cm^3 of PSL particles). That is, the deviations of $D_{ve,me}$

207   and $\rho_{e,me}$ characterized by the AAC-SPAMS system are within 1% and 6%, respectively.

208   We therefore conclude that the AAC-SPAMS system is highly accurate for obtaining

209   aerosol D_{ve} and ρ_e.

210

3.2 Application of the AAC-SPAMS system for obtaining D_{ve} and ρ_e of (NH$_4$)$_2$SO$_4$ and NaNO$_3$

Figure S2 shows the D_{va} distributions of (NH$_4$)$_2$SO$_4$ and NaNO$_3$ particles, which have D_a values of 250.0, 350.0, 450.0, and 550.0 nm, as screened by the AAC. The D_{va} peaks are obtained by Gaussian fitting, with R^2 values over 0.93 and FWHM values ranging from 7.6% to 10.6%. The (NH$_4$)$_2$SO$_4$ particles have D_{va} values of 300.0, 418.0, 551.1, and 695.1 nm (Figure S2), which correspond to particles possessing $D_{ve,me}$ values of 177.3, 254.4, 331.8, and 409.3 nm, respectively, according to Eq. (11). Substituting the values of D_{va} and $D_{ve,me}$ into Eq. (12), the $\rho_{e,me}$ values are 1.7, 1.6, 1.6, and 1.7 g/cm^3 (Figure 3a), respectively. Similarly, the selected NaNO$_3$ particles are determined to have D_{va} values of 321.0, 454.9, 599.8, and 755.3 nm (Figure S2), corresponding to $D_{ve,me}$ values of 150.1, 218.2, 287.0, and 355.9 nm, respectively. The $\rho_{e,me}$ values of the NaNO$_3$ particles are 2.2, 2.0, 2.0, and 2.1 g/cm^3 for the four particle sizes (Figure 3b), respectively. Figure 3 also shows that the $\rho_{e,me}$ values of the NaNO$_3$ and (NH$_4$)$_2$SO$_4$ particles at four size deviate from their average values with the maximum of 5.9 % and 4.8%, respectively, which are identical with the deviation phenomenon for the $\rho_{e,me}$ of PSL particles. These deviations may be derived from the calibration of particle Dva from the SPAMS. While the R-square of size calibration curve is 0.999, the curve of exponential function is found to slightly deviate from the data points measured by SPAMS. For example, size calibration function has the deviation of -4.4% and 3.1% from the data points of 310 and 740 nm, respectively.

Taking the systematic error into account, the slight difference of the $\rho_{e,me}$ values for

233   the four sizes suggests that the ρ_e of $(NH_4)_2SO_4$ and $NaNO_3$ particles is independent of

234   particle size from 250.0 nm to 550.0 nm. It is determined by the definition of effective

235   density used in this study, which keeps constant as long as the χ_a of the particles does

236   not change with particle size for pure compound. The average $\rho_{e,me}$ values of $(NH_4)_2SO_4$

237   and $NaNO_3$ particles are calculated to be 1.7 ± 0.1 and 2.1 ± 0.1 g/cm^3, respectively.

238   The average $\rho_{e,me}$ values are lower than that the ρ_p of $(NH_4)_2SO_4$ (1.77 g/cm^3) and

239    $NaNO_3$ (2.27 g/cm^3), which is caused that the $\rho_{e,me}$ is determined by both of ρ_p and χ_a.

240   According to Eq. (14), the χ_a of $(NH_4)_2SO_4$ and $NaNO_3$ particles with different D_a are

241   calculated to be 1.04, 1.11, 1.11, and 1.04 and to be 1.03, 1.14, 1.14, and 1.08,

242   respectively. Thus, the average χ_a values of the $(NH_4)_2SO_4$ and $NaNO_3$ particles are

243   determined to be 1.07 ± 0.04 and 1.10 ± 0.05, respectively, which can be used to

244   parameterize their morphology.

245   The average χ_a values of the $(NH_4)_2SO_4$ and $NaNO_3$ particles indicate that these

246   particles are aspherical. The asphericity of $(NH_4)_2SO_4$ determined by AAC-SPAMS

247   system is consistent with the previous studies reporting that the χ_a of $(NH_4)_2SO_4$ were

248   larger than the value of 1.03 (Zelenyuk et al., 2006;Beranek et al., 2012;Zhang et al.,

249   2016a). However, previous studies found that the $NaNO_3$ particles had different

250   morphology. Zhang et al. (2016a) observed that $NaNO_3$ had the χ_a of 1.09-1.13,

251   indicating its asphericity, while Hoffman et al. (2004) found that $NaNO_3$ particle had a

252   round droplet-like shape even at 15% RH, which was supported by the consistence

253   between the measured value of "anhydrous" droplet density and the calculated value of

254   "anhydrous" solution droplet (Zelenyuk et al., 2005). Eclectically, Tang and

255 Munkelwitz (1994) studied that most of the $NaNO_3$ particles crystallized between 20%

256 and 30% RH but some persisted down to 10% RH to form solution droplets. Notably,

257 the spherical $NaNO_3$ particles at low RH observed by Hoffman et al. (2004) were dried

258 in the sticky carbon tape which might affect the phase transition of droplet-like $NaNO_3$

259 particles. In this study, most $NaNO_3$ particles were crystallized because the RH of the

260 aerosol flow carrying the $NaNO_3$ particles was reduced to below 20% through the

261 diffusion drying tube. Besides, the result that the crystallized $NaNO_3$ particles are

262 aspherical is supported by their FWHM values of the D_{va} distributions which are

263 consistent with that of aspherical $(NH_4)_2SO_4$ but wider than spherical PSL (Figures S1

264 and S2).

265

266 **3.3 Application of the AAC-SPAMS system for measuring the chemically-resolved**

267 D_{ve} **and** ρ_e

268   SPAMS can obtain information on the chemical composition of individual particles,

269 implying that the AAC-SPAMS system has the ability to simultaneously characterize

270 D_{ve}, ρ_e and the chemical compositions of particles in real time. It is worth noting that

271 the particles with the largest χ in the actual atmosphere should be freshly emitted soot,

272 which χ is 2.5 (Peng et al., 2016). This largest χ fitly meets the upper limit for the

273 approximation between the χ_t and χ_v (DeCarlo et al., 2004). Therefore, the AAC-SPAMS

274 system can obtain the chemically-resolved D_{ve} and ρ_e values for unknown aerosol

275 particles in the field observation.

276   As an example, we applied the AAC-SPAMS system to illustrate how the measured

277   D_a, D_{va}, and chemical composition of an individual particle can be used to calculate the

278   D_{ve} and ρ_e for unknown particles. The sampled ~100,000 particles are classified into

279   eight major particle types with distinct chemical patterns of K-rich, EC-S, K-Na, Amine,

280   EC-N-S, OC-N-S and OC-EC-N-S and Metal-rich, representing 97% of the detected

281   particle population. Details of the chemical composition and number fraction of the

282   eight types of particles are presented in the Figure S3 and Figure S4, respectively, which

283   are discussed in the Supporting Information.

284   We used Gaussian fitting to obtain the D_{va} peaks for each particle type with D_a values

285   of 250.0 nm, 350.0 nm, 450.0 nm, and 550.0 nm. Then, we calculated the D_{ve} values of

286   the atmospheric particles with Eq. (11). Table 1 presents the average D_{ve} values of the

287   eight particle types, for which the standard deviation is calculated based on nine

288   samples. The average D_{ve} at D_a values of 250.0 nm, 350.0 nm, 450.0 nm, and 550.0 nm

289   has the following wide ranges: from 188.5 nm to 200.8 nm, 271.9 nm to 295.7 nm,

290   342.5 nm to 428.9 nm, and 397.3 nm to 570.9 nm, respectively, which are caused by

291   the chemical composition differences. The result indicates that particles with

292   significantly different D_{ve} might possess the same D_a. Furthermore, the large standard

293   deviation of D_{ve}, such as 21.9 nm for K-Na at 250.0 nm, 32.3 nm for OC-EC-N-S at

294   350.0 nm, and 44.3 nm for OC-N-S at 450.0 nm, indicates that the D_{ve} of particles is

295   remarkably different even for particles with the same type and same D_a.

296   According to D_{ve} and D_{va}, we calculated the ρ_e of each particle type with Eq. (12).

297   Figure 4 shows the variations of the ρ_e with D_{ve} for nine particle samples. For pure

298   compounds, such as $(NH_4)_2SO_4$ and $NaNO_3$ particle, ρ_e theoretically does not change

299 with particle size. However, the sampled particles have experienced complex

300 atmospheric processes. Therefore, ρ_e has a very wide distribution for each type of

301 particle with a similar D_{ve}. Specifically, the ρ_e of K-Na increases with D_{ve}, while the ρ_e

302 of OC-N-S and OC-EC-N-S decreases with D_{ve}, which may be influenced by the

303 particle shape or the material density. Additionally, the average ρ_e of each type of

304 particle is in the order from small to large: 1.2 ± 0.2 g/cm^3 for OC-EC-N-S, 1.3 ± 0.2

305 g/cm^3 for OC-N-S, 1.4 ± 0.1 g/cm^3 for K-rich, 1.4 g/cm^3 for Amine, 1.5 g/cm^3 for EC-

306 N-S, 1.5 g/cm^3 for EC-S, 1.6 ± 0.1 g/cm^3 for K-Na and 1.6 ± 0.1 g/cm^3 for Metal-rich.

307 It is reasonable to find that the average ρ_e of internally mixed particles distributes in the

308 range of their material densities (ρ_m). For instance, mainly comprised of internally

309 mixed sulfate and organics, the OC-EC-N-S, OC-N-S, K-rich, and Amine particles have

310 the average ρ_e between that of sulfate with ρ_m of 1.77 g/cm^3 and organic aerosols with

311 ρ_m of 1.2 g/cm^3 (Cross et al., 2007).

312

313 **4. Conclusion**

314 We first develop an AAC-SPAMS system to achieve the measurement of the D_{ve} and

315 ρ_e of the particles through characterizing their D_a and D_{va}. The reliability of the AAC-

316 SPAMS system is verified by accurately measuring the D_{ve} and ρ_e of PSL. Applying the

317 AAC-SPAMS system to determine the D_{ve} and ρ_e of (NH$_4$)$_2$SO$_4$ and NaNO$_3$ particles

318 shows that these particles are aspherical and their ρ_e are independent of particle size.

319 Coupled with the ability of SPAMS to characterize the chemical composition of

320 individual particles, we conducted a sample proof of the AAC-SPAMS equipment in

321 Guangzhou to first characterize the D_{ve}, ρ_e and chemical compositions of atmospheric

322 particles, showing the potential application of this system in field observations. The

323 approach achieves the measurement of chemically-resolved D_{ve} and ρ_e, and provides

324 the possibility to determine their quantitative relationship with other particle properties,

325 which would be benefit for further reduction of the uncertainty associated with the

326 effects of particles on air quality, human health and radiative forcing.

327

328 ***Data availability.*** Data in this study is available at https://github.com/longer1217/All-

329 figures-data.

330

331 ***Author contributions.*** The idea for the study was conceived by LP and GHZ. All

332 experiments were performed by LP with the assistance of LL. LP wrote the paper which

333 was reviewed by GHZ and XHB. All co-authors discussed the results and commented

334 on the manuscript.

335

336 **Competing interests.** The authors declare they have no conflict of interest.

337

338 **Acknowledgment**

339   This work was supported by the National Nature Science Foundation of China

340 (41775124 and 41877307), Natural Science Foundation of Guangdong Province

341 (2019B151502022), and the Guangdong Foundation for the Program of Science and

342 Technology Research (2019B121205006 and 2017B030314057). The authors also

343   gratefully acknowledge Cambustion Ltd., UK for providing the AAC and Hexin

344   Analytical Instrument Co., Ltd., China for providing the SPAMS.

345

346   **References**

347   Beranek, J., Imre, D., and Zelenyuk, A.: Real-time shape-based particle separation and

348   detailed in situ particle shape characterization, Anal. Chem., 84, 1459-1465,

349   https://doi.org/10.1021/ac202235z, 2012.

350   Buseck, P. R., and Posfai, M.: Airborne minerals and related aerosol particles: effects

351   on climate and the environment, P. Natl. Acad. Sci. USA, 96, 3372-3379,

352   https://doi.org/10.1073/pnas.96.7.3372, 1999.

353   Cross, E. S., Slowik, J. G., Davidovits, P., Allan, J. D., Worsnop, D. R., Jayne, J. T.,

354   Lewis, D. K., Canagaratna, M., and Onasch, T. B.: Laboratory and ambient particle

355   density determinations using light scattering in conjunction with aerosol mass

356   spectrometry, Aerosol Sci. and Technol., 41, 343-359,

357   https://doi.org/10.1080/02786820701199736, 2007.

358   DeCarlo, P. F., Slowik, J. G., Worsnop, D. R., Davidovits, P., and Jimenez, J. L.: Particle

359   morphology and density characterization by combined mobility and aerodynamic

360   diameter measurements. Part 1: Theory, Aerosol Sci. and Technol., 38, 1185-1205,

361   https://doi.org/10.1080/027868290903907, 2004.

362   Guo, S., Hu, M., Zamora, M. L., Peng, J. F., Shang, D. J., Zheng, J., Du, Z. F., Wu, Z.,

363   Shao, M., Zeng, L. M., Molina, M. J., and Zhang, R. Y.: Elucidating severe urban

364   haze formation in China, P. Natl. Acad. Sci. USA, 111, 17373-17378, 2014.

365   Hand, J. L., and Kreidenweis, S. M.: A new method for retrieving particle refractive

366   index and effective density from aerosol size distribution data, Aerosol Sci. and

367   Technol., 36, 1012-1026, https://doi.org/10.1080/02786820290092276, 2002.

368   Hoffman, R. C., Laskin, A., and Finlayson-Pitts, B. J.: Sodium nitrate particles: physical

369   and chemical properties during hydration and dehydration, and implications for

370   aged sea salt aerosols, J. Aerosol Sci., 35, 869-887, 2004.

371   Katrib, Y., Martin, S. T., Rudich, Y., Davidovits, P., Jayne, J. T., and Worsnop, D. R.:

372   Density changes of aerosol particles as a result of chemical reaction, Atmos. Chem.

373   Phys., 5, 275-291, https://doi.org/10.5194/acp-5-275-2005, 2005.

374   Li, L., Huang, Z. X., Dong, J. G., Li, M., Gao, W., Nian, H. Q., Fu, Z., Zhang, G. H.,

375   Bi, X. H., Cheng, P., and Zhou, Z.: Real time bipolar time-of-flight mass

376   spectrometer for analyzing single aerosol particles, Int. J. Mass Spectrom., 303,

377   118-124, https://doi.org/10.1016/j.ijms.2011.01.017, 2011.

378   Liu, Y., and Daum, P. H.: Relationship of refractive index to mass density and self-

379   consistency of mixing rules for multicomponent mixtures like ambient aerosols, J.

380   Aerosol Sci., 39, 974-986, https://doi.org/10.1016/j.jaerosci.2008.06.006, 2008.

381   Liu, Z., Hu, B., Ji, D., Wang, Y., Wang, M., and Wang, Y.: Diurnal and seasonal variation

382   of the PM2.5 apparent particle density in Beijing, China, Atmos. Environ., 120,

383   328-338, https://doi.org/10.1016/j.atmosenv.2015.09.005, 2015.

384   Moffet, R. C., and Prather, K. A.: Extending ATOFMS measurements to include

385   refractive index and density, Anal. Chem. 77, 6535-6541,

386   https://doi.org/10.1021/ac0503097, 2005.

387   Moffet, R. C., Qin, X., Rebotier, T., Furutani, H., and Prather, K. A.: Chemically

388   segregated optical and microphysical properties of ambient aerosols measured in

389   a single-particle mass spectrometer, J. Geophys. Res.-Atmos., 113,

390   https://doi.org/10.1029/2007jd009393, 2008.

391   Peng, J. F., Hu, M., Guo, S., Du, Z. F., Zheng, J., Shang, D. J., Zamora, M., Zeng, L.

392   M., Shao, M., Wu, Y. S., Zheng, J., Wang, Y., Glen, C., Collins, D., Molina, M.,

393   and Zhang, R. Y.: Markedly enhanced absorption and direct radiative forcing of

394   black carbon under polluted urban environments, P. Natl. Acad. Sci. USA, 252,

395   2016.

396   Pitz, M., Cyrys, J., Karg, E., Wiedensohler, A., Wichmann, H. E., and Heinrich, J.:

397   Variability of apparent particle density of an urban aerosol, Environ. Sci. &

398   Technol., 37, 4336-4342, https://doi.org/10.1021/es034322p, 2003.

399   Poschl, U.: Atmospheric aerosols: Composition, transformation, climate and health

400   effects, Angew. Chem. Int. Edit., 44, 7520-7540,

401   https://doi.org/10.1002/anie.200501122, 2005.

402   Schneider, J., Weimer, S., Drewnick, F., Borrmann, S., Helas, G., Gwaze, P., Schmid,

403   O., Andreae, M. O., and Kirchner, U.: Mass spectrometric analysis and

404   aerodynamic properties of various types of combustion-related aerosol particles,

405   Int. J. Mass Spectrom., 258, 37-49, https://doi.org/10.1016/j.ijms.2006.07.008,

406   2006.

407   Seinfeld, J. H., and Pandis, S. N.: From air pollution to climate change, 429-443, 1998.

408   Song, X. H., Hopke, P. K., Fergenson, D. P., and Prather, K. A.: Classification of single

409    particles analyzed by ATOFMS using an artificial neural network, ART-2A, Anal.

410    Chem., 71, 860-865, https://doi.org/10.1021/ac9809682, 1999.

411  Sumlin, B. J., Oxford, C. R., Seo, B., Pattison, R. R., Williams, B. J., and Chakrabarty,

412    R. K.: Density and homogeneous internal composition of primary brown carbon

413    Aerosol, Environ. Sci. & Technol., 52, 3982-3989,

414    https://doi.org/10.1021/acs.est.8b00093, 2018.

415  Tang, I. N., and Munkelwitz, H. R.: Water activities, densities, and refractive-indexes

416    of aqueous sulfates and sodium-nitrate droplets of atmospheric importance, J.

417    Geophys. Res.-Atmos., 99, 18801-18808, 1994.

418  Tang, I. N.: Thermodynamic and optical properties of mixed-salt aerosols of

419    atmospheric importance, J. Geophys. Res.-Atmos., 102, 1883-1893, 1997.

420  Tavakoli, F., and Olfert, J. S.: An instrument for the classification of aerosols by particle

421    relaxation time: theoretical models of the aerodynamic aerosol classifier, Aerosol

422    Sci. and Technol., 47, 916-926, https://doi.org/10.1080/02786826.2013.802761,

423    2013.

424  Yin, Z., Ye, X. N., Jiang, S. Q., Tao, Y., Shi, Y., Yang, X., and Chen, J. M.: Size-resolved

425    effective density of urban aerosols in Shanghai, Atmos. Environ., 100, 133-140,

426    https://doi.org/10.1016/j.atmosenv.2014.10.055, 2015.

427  Yon, J., Bescond, A., and Ouf, F. X.: A simple semi-empirical model for effective

428    density measurements of fractal aggregates, J. Aerosol Sci., 87, 28-37,

429    https://doi.org/10.1016/j.jaerosci.2015.05.003, 2015.

430  Zelenyuk, A., Cai, Y., Chieffo, L., and Imre, D.: High precision density measurements

431   of single particles: The density of metastable phases, Aerosol Sci. and Technol.,

432   39, 972-986, https://doi.org/10.1080/02786820500380206, 2005.

433 Zelenyuk, A., Cai, Y., and Imre, D.: From agglomerates of spheres to irregularly shaped

434   particles: Determination of dynamic shape factors from measurements of mobility

435   and vacuum aerodynamic diameters, Aerosol Sci. and Technol., 40, 197-217,

436   https://doi.org/10.1080/02786820500529406, 2006.

437 Zhang, G., Bi, X., Han, B., Qiu, N., Dai, S., Wang, X., Sheng, G., and Fu, J.:

438   Measurement of aerosol effective density by single particle mass spectrometry,

439   Science China Earth Sciences, 59, 320-327, https://doi.org/10.1007/s11430-015-

440   5146-y, 2016a.

441 Zhao, G., Zhao, W., and Zhao, C.: Method to measure the size-resolved real part of

442   aerosol refractive index using differential mobility analyzer in tandem with single-

443   particle soot photometer, Atmos. Meas. Tech., 12, 3541-3550,

444   https://doi.org/10.5194/amt-12-3541-2019, 2019.

445

446   **Table 1.** D_{ve} and its standard deviation for the eight particle types at D_a values of 250.0 nm, 350.0
447   nm, 450.0 nm, and 550.0 nm from nine round measurement.
448

D_a (nm)	K-rich	EC-S	K-Na	Amine
250.0	193.1 ± 8.2	192.2 ± 8.1	193.8 ± 21.9	190.6 ± 4.6
350.0	284.0 ± 28.4	280.8 ± 9.3	271.9 ± 18.0	284.8 ± 18.2
450.0	364.7 ± 21.1	357.8 ± 6.9	342.5 ± 7.3	367.9 ± 9.7
550.0	416.6 ± 28.3	439.5 ± 5.4	397.3 ± 29.7	442.5 ± 7.4
D_a (nm)	EC-N-S	OC-N-S	OC-EC-N-S	Metal-rich
250.0	188.5 ± 5.9	200.8 ± 17.9	195.4 ± 8.9	189.0 ± 6.7
350.0	281.3 ± 9.3	295.7 ± 29.8	294.0 ± 32.3	277.0 ± 9.1
450.0	358.0 ± 5.8	398.3 ± 44.3	428.9 ± 24.0	342.9 ± 10.0
550.0	453.2 ± 16.4	547.4 ± 14.7	570.9	407.4 ± 14.5

449
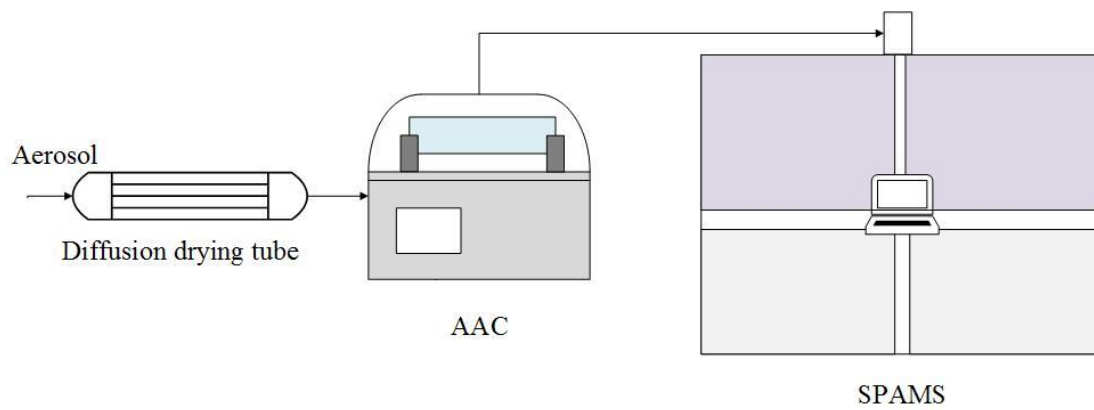
450

451   **Figure 1.** Schematic diagram of the AAC-SPAMS system (0.3 lpm). The diffusion drying tube is

452   filled with orange silica gel, which reduces the RH to 5-15%.
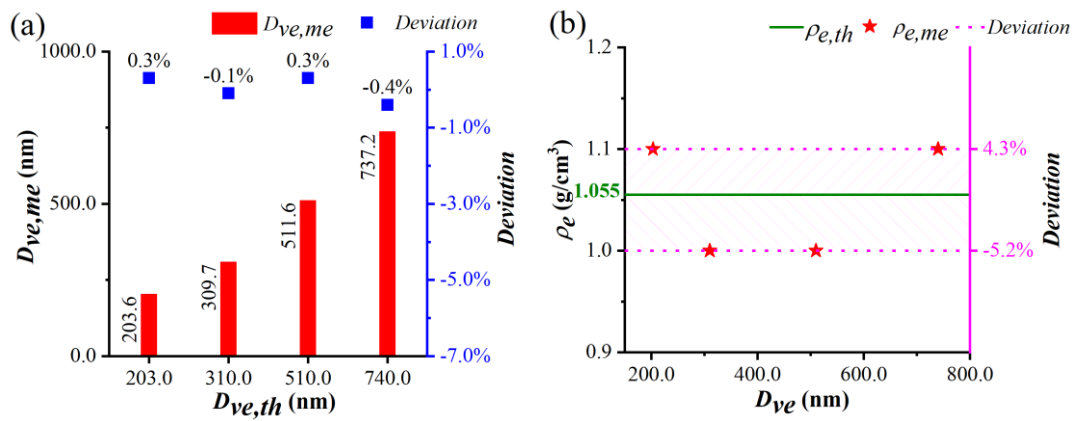
Figure 2. (a) Comparison between the measured D_{ve} ($D_{ve,me}$) and the theoretical D_{ve} ($D_{ve,th}$) of the

PSL particles. (b) Comparison between the measured ρ_e ($\rho_{e,me}$) and the theoretical ρ_e ($\rho_{e,th}$) of the
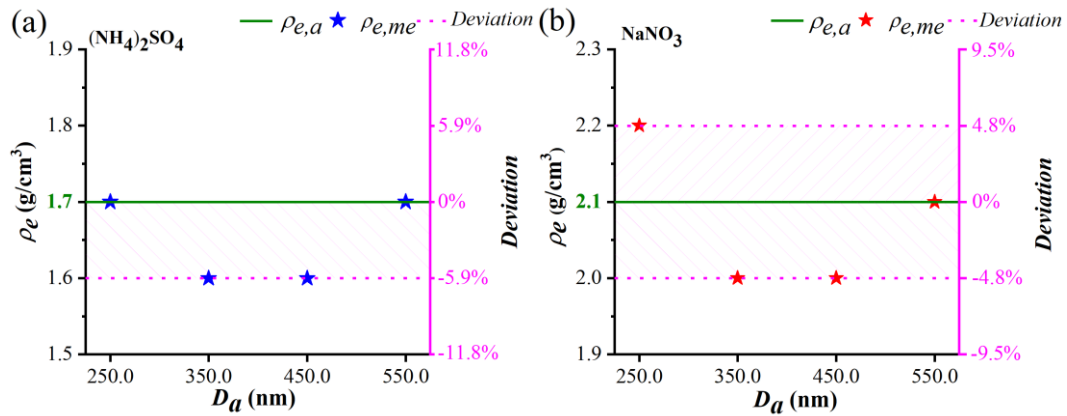
PSL particles.

458

459

460 **Figure 3.** (a) Comparison between the measured ρ_e ($\rho_{e,me}$) and average ρ_e ($\rho_{e,a}$) values of the

461 $(NH_4)_2SO_4$ particles. (b) Comparison between the measured ρ_e ($\rho_{e,me}$) and average ρ_e ($\rho_{e,a}$) values of

462 the $NaNO_3$ particles.
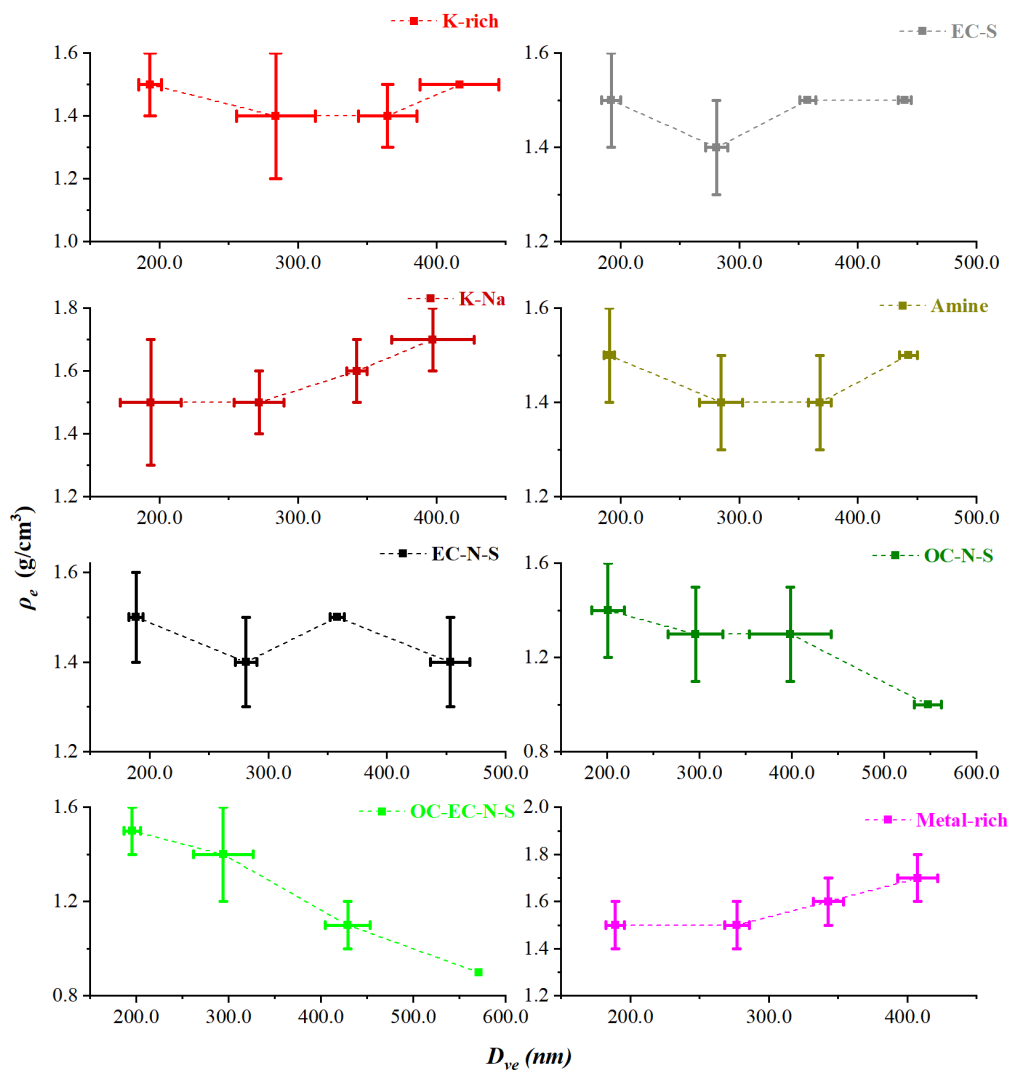
Figure 4. Variation in ρ_e of the eight particle types with D_{ve}. The solid lines represent the rang of the ρ_e and D_{ve} measured from nine rounds, and the data points stand for the average values.